



The Mean Magnetic Field Strength of CI Tau

Kimberly R. Sokal¹ , Christopher M. Johns-Krull², Gregory N. Mace¹ , Larissa Nofi³, L. Prato³, Jae-Joon Lee⁴ , and Daniel T. Jaffe¹

¹ Department of Astronomy, The University of Texas at Austin, Austin, TX, 78712, USA; ksokal@utexas.edu

² Department of Physics and Astronomy, Rice University, 6100 Main Street, MS-108, Houston, TX 77005, USA

³ Lowell Observatory, 1400 W. Mars Hill Road, Flagstaff, AZ 86001, USA

⁴ Korea Astronomy and Space Science Institute, 776 Daedeokdae-ro, Yuseong-gu, Daejeon 34055, Republic of Korea

Received 2019 January 12; revised 2019 October 6; accepted 2019 October 31; published 2020 January 15

Abstract

We present a blind comparison of two methods to measure the mean surface magnetic field strength of the classical T Tauri star CI Tau based on Zeeman broadening of sensitive spectral lines. Our approach takes advantage of the greater Zeeman broadening at near-infrared compared to optical wavelengths. We analyze a high signal-to-noise, high spectral resolution spectrum from 1.5 to 2.5 μm observed with IGRINS (Immersion GRating INfrared Spectrometer) on the Discovery Channel Telescope. Both stellar parameterization with MoogStokes (which assumes a uniform magnetic field) and modeling with SYNTHMAG (which includes a distribution of magnetic field strengths) yield consistent measurements for the mean magnetic field strength of CI Tau is B of ~ 2.2 kG. This value is typical compared with measurements for other young T Tauri stars and provides an important contribution to the existing sample given that it is the only known developed planetary system hosted by a young classical T Tauri star. Moreover, we potentially identify an interesting and suggestive trend when plotting the effective temperature and the mean magnetic field strength of T Tauri stars. While a larger sample is needed for confirmation, this trend only appears for a subset of the sample, which may have implications regarding the magnetic field generation.

Unified Astronomy Thesaurus concepts: [Infrared sources \(793\)](#); [Fundamental parameters of stars \(555\)](#); [Stellar magnetic fields \(1610\)](#); [Pre-main-sequence stars \(1290\)](#)

Supporting material: data behind figures

1. Introduction

Strong stellar magnetic fields play a fundamental role in the pre-main-sequence (PMS) and early main-sequence evolution of late-type stars. It is now well-established that the interaction of the newly formed star, also known as a T Tauri star (TTS), with its disk is strongly regulated by the stellar magnetic field. This interaction is described principally by the magnetospheric accretion paradigm (Bouvier et al. 2007). In magnetospheric accretion, the large scale component of the stellar field truncates the accretion disk at or near the co-rotation radius, redirecting the path of accreting disk material so that it flows along the stellar magnetic field lines to the surface of the star. It is usually assumed that the footprints of the stellar magnetic field, which take part in the accretion process, are anchored at high latitude so that accretion occurs near the stellar poles. When the accreting material impacts the stellar surface, it experiences a strong shock, heating up to $\sim 10^6$ K (Calvet & Gullbring 1998). In addition to accretion of disk material, disk bearing young stars also experience strong outflows (e.g., Hartigan et al. 1995; Edwards et al. 2006), which the stellar magnetic field likely plays an important role in launching (e.g., Shu et al. 1994; Romanova et al. 2009; Zanni & Ferreira 2013). Most of the observational signatures that define classical TTSs (CTTSs) are produced by emissions from the gas taking part in these accretion and outflows, which are mediated by the stellar magnetic field.

In addition to mediating the outflows and accretion of disk material onto young stars, the stellar magnetic field plays a significant role in the rotational evolution of solar type stars. As a young star contracts during its PMS evolution, the

conservation of angular momentum would cause the rotation rate of the star to increase. However, during the CTTS phase, the rotation of the young star appears to become locked to that of the disk at or near the truncation radius (e.g., Edwards et al. 1993; Johns-Krull & Gafford 2002; Rebull et al. 2006; Cieza & Baliber 2007; Cauley et al. 2012). The value of the truncation radius depends on the strength and geometry of the stellar magnetic field, on the disk accretion rate, and also on the stellar mass through its influence on the velocity of orbiting material (Elsner & Lamb 1977; Ghosh & Lamb 1979; Hartmann 1998; Bessolaz et al. 2008). While some authors question whether the action of the stellar magnetic field is sufficient to supply the needed torque and enforce disk locking (Uzdensky et al. 2002; Matt & Pudritz 2005; Matt et al. 2010; Aarnio et al. 2013), and other studies do not always find a clear observational signature of disk locking (Rebull 2001; Stassun et al. 2001), current models of PMS angular momentum evolution require disk locking or some similar process to reproduce the observed distribution of rotation periods in young clusters (e.g., Bouvier et al. 1997; Krishnamurthi et al. 1997; Barnes et al. 2001; Tinker et al. 2002; Irwin et al. 2008; Gallet & Bouvier 2013, 2015). To match the range of observed rotation periods in young clusters, most studies find that disk locking must act over a range of times in the early evolution of TTSs, which is consistent with the observed falloff of disk fraction in young star-forming regions (Haisch et al. 2001; Hernández et al. 2007; Wyatt 2008). Once the disks vanish and the young star has contracted to the main sequence, the stellar field remains important for rotational evolution through the action of a magnetized stellar wind, which spins the star down over the

course of a few Gyr (e.g., Weber & Davis 1967; Skumanich 1972; Matt et al. 2015).

In addition to their importance in the rotational evolution of newly formed stars, strong stellar fields are also critical for our understanding of stellar ages and have implications for planetary systems. Planets form in the disks around young stars (Chabrier et al. 2014; Johansen et al. 2014; Raymond et al. 2014). Therefore, the timescale for planet formation, planet migration, and other processes in the protoplanetary disk that help determine the final architecture of planetary systems is set by the lifetime of the disk. The disk lifetimes are found by measuring the age of newly formed stars (e.g., Hernández et al. 2007), and uncertainties in stellar ages translate directly into uncertainties in disk lifetimes. A number of studies have now established that ubiquitous, strong stellar magnetic fields can measurably alter the structure of low-mass stars (Mullan & MacDonald 2001; Chabrier et al. 2007; MacDonald & Mullan 2009; Torres et al. 2010), including TTs (Feiden & Chaboyer 2013, 2014; Feiden 2016). The resulting change in stellar evolution can produce a factor of two discrepancy in the age of young stars at the few million year timeframe, which could possibly explain the difference in age found for some clusters (Pecaut et al. 2012) when the age is determined from the intermediate to high mass stars compared to the low-mass stars (Feiden 2016). Consequently, understanding the magnetic field properties of young stars is critical for establishing timescales involved in planet formation. A related effect comes from the influence that magnetic fields can have on the ability to properly place young stars in a Hertzsprung–Russell (HR) diagram and determine their ages by comparing to model PMS evolutionary tracks. It is often desirable to use spectroscopic techniques to measure the effective temperature and/or gravity to aid in placing stars in the HR diagram, and failing to account for strong stellar magnetic fields can still result in significant systematic offsets on where stars appear in the HR diagram (e.g., Doppmann et al. 2003; Sokal et al. 2018). This can be particularly important when using near-infrared (NIR) spectra, and is advantageous for cool and embedded sources because the wavelength dependence of the Zeeman effect makes NIR atomic lines particularly sensitive to, and therefore strongly affected by, magnetic fields (e.g., Saar & Linsky 1985; Johns-Krull et al. 1999; Johns-Krull 2007).

Furthermore, magnetic fields may have important effects on the planet formation process itself, for example the observed pileup of planets on very close orbits and the likelihood of planets being habitable. Hot Jupiters, roughly Jupiter-mass planets in very close orbits around their host stars, have a peak in their distribution at ~ 0.04 au (e.g., Baruteau et al. 2014; Heller 2018). It is now well-accepted that these planets must form significantly further out in the disk and then migrate in through some mechanism (Lin & Papaloizou 1986; Papaloizou et al. 2007; Triaud et al. 2010; Naoz et al. 2011). The stellar magnetosphere can cause inner disk truncation, which then halts inward migration and leads to a pileup of hot Jupiters (e.g., Lin et al. 1996; Chang et al. 2010; Ida & Lin 2010; Plavchan & Bilinski 2013; Baruteau et al. 2014). High energy radiation resulting from the stellar magnetic activity also potentially plays an important role in disk ionization structure and chemistry (e.g., Glassgold et al. 1997, 2004; Dullemond & Monnier 2010; Ádámkóvics et al. 2014), which influences the environment where planets form and potentially migrate. Once planets do form, the stellar magnetic field likely plays a

significant role in the potential habitability of worlds around other stars, again through the impact of high energy radiation resulting from the magnetic activity, which is then incident on planetary atmospheres (e.g., Kaltenegger et al. 2010; Segura et al. 2010; Tilley et al. 2017). Consequently, it is important to know the magnetic properties of young stars that are in the process of forming, or have recently formed, planets.

Planetary mass companions in close orbits around their host stars have so far been identified through radial velocity (RV) and transit searches. Both RV and transit search studies of young stars are significantly impacted by astrophysical noise resulting from the extreme stellar and accretion activity of young stars (Paulson & Yelda 2006; Desort et al. 2007; Huélamo et al. 2008; Prato et al. 2008; Mahmud et al. 2011). Hampered by this noise, some claimed detections have later been found to be the results of stellar activity. Nevertheless, there have been a number of RV and transit surveys for planets around young low-mass stars (Setiawan et al. 2007, 2008; Hernán-Obispo et al. 2010; van Eyken et al. 2011; Bailey et al. 2012; Crockett et al. 2012; Nguyen et al. 2012; Lagrange et al. 2013; Gagné et al. 2016). To date, only a handful of high-quality planet candidates in close orbits around young (≤ 10 Myr) parent stars have been announced (van Eyken et al. 2012; David et al. 2016; Donati et al. 2016; Johns-Krull et al. 2016; Yu et al. 2017). Only one of these planet candidates, CI Tau b, is around a CTTS (Johns-Krull et al. 2016), offering the possibility to study a system where a star, its disk, and a massive planet can interact. An additional very low-mass brown dwarf ($m_{\text{sin}} \approx 19 M_{\text{JUP}}$) has been discovered around the CTTS AS 205 A (Almeida et al. 2017).

Johns-Krull et al. (2016) announced CI Tau b as an $\sim 11 M_{\text{JUP}}$ planet in a possibly eccentric orbit around the CTTS CI Tau. Biddle et al. (2018) examined the K2 lightcurve of CI Tau and found additional support for the planetary interpretation of the RV signals observed by Johns-Krull et al. (2016). Even more recently, Clarke et al. (2018) used ALMA to find evidence for three additional gas giant planets orbiting CI Tau. As an ~ 2 Myr old star with fairly mature suite of planets, this system may have much to reveal about planet formation and migration.

One important parameter of the CI Tau system that has yet to be probed is the stellar magnetic field of CI Tau. Here, we seek to measure the global magnetic field properties of this star, focusing on the average strength of the magnetic field at the stellar surface. Zeeman broadening of K-band Ti I lines is an excellent way to measure the magnetic field strength on low-mass young stars (Johns-Krull et al. 1999; Johns-Krull 2007) and has been used to measure the field strengths of close to three dozen young systems to date. In addition to characterizing the CI Tau magnetic field, we also compare two methods that are now used in the literature to measure the fields of low-mass, young stars. Most studies of the Zeeman broadening of NIR Ti I lines follow the analysis described by Johns-Krull et al. (1999) and Johns-Krull (2007), and they use the SYNTHMAG code (Piskunov 1999) to fit a distribution of magnetic field strengths on the stellar surface. Recently, Deen (2013) modified the MOOG (Snedden 1973) LTE atmospheres code to perform radiative transfer in the presence of a magnetic field. Sokal et al. (2018) used this code to analyze high resolution NIR spectra of the CTTS TW Hya and measure its mean magnetic field, finding a value 3.0 kG. Yang et al. (2005) used SYNTHMAG to fit a distribution of field strengths on the

Table 1
IGRINS Observations of CI Tau

UT Date	Integration Time	Observing Sequence	Airmass	A0V Telluric Standard
20161016	300	ABBA	1.07	HIP 21823
20161111 ^a	300	ABBA	1.035	HIP 21823
20161112	300	ABBA x 2	1.03	HIP 18769
20161115	300	ABBA	1.195	HIP 23088
20161125	600	ABBA x 2	1.14	HIP 23088
20161126	300	ABBA x 2	1.205	HIP 23088
20161208	500	ABBAAB	1.02	HIP 21823
20170911	180	ABBA x 3	1.275	HIP 23088
20170913	300	ABBA x 2	1.24	HIP 23088
20170916	300	ABBA x 2	1.145	HIP 23088

Note.

^a Reference visit.

stellar surface, finding a mean field strength of 2.7 kG. These two studies used spectra taken with different instruments at different times; therefore, while it is encouraging that they find similar mean magnetic fields, the agreement between the two analysis techniques has not been properly tested. We seek to perform such a test in this paper. The remainder of this paper contains a description of the observations and data reduction in Section 2, a description of the analysis in Section 3, a discussion of the results in Section 4, and our conclusions are presented in Section 5.

2. Observations and Data Reduction

We present a high signal-to-noise IGRINS spectrum of CI Tau, produced by combining IGRINS spectra from 10 separate visits. IGRINS (Immersion GRating INfrared Spectrometer) is an extremely powerful instrument that provides a large spectral grasp with high throughput. IGRINS spectra cover the entire *H*- and *K*-bands (1.45–2.5 μm) with a resolving power of $R = \frac{\lambda}{\delta\lambda} = 45,000$ (Park et al. 2014; Mace et al. 2016, 2018). The 10 observations of CI Tau were obtained with IGRINS on the 4.3 m Discovery Channel Telescope of Lowell Observatory over the years of 2016–2017. See Table 1 for a complete list of the observations. The airmass of CI Tau varied per visit and ranged from 1.02 to 1.275. An A0V telluric standard was observed at a similar airmass, either prior or following CI Tau on every night. All targets were nodded along the slit in AB and BA patterns.

To reduce each visit’s IGRINS spectroscopic dataset, we use the IGRINS pipeline package (version 2.1 alpha 3; Lee & Gullikson 2016) to produce a one-dimensional, telluric-corrected spectrum with wavelength solutions derived from OH night sky emission lines at shorter wavelengths and telluric absorption lines at wavelengths greater than 2.2 μm . The telluric correction is then performed by dividing the target spectrum by the A0V telluric standard and multiplying by a standard Vega model. The uncertainties of the telluric-corrected spectra are derived by adding the observed uncertainties of the target and standard spectra in quadrature. In addition to increasing signal, another benefit of combining visits later is that residuals from the telluric correction process are eliminated or greatly reduced, as are most noise elements. Lastly, we correct for the barycenter velocity that corresponds to the Julian time at the middle of each observation.

In preparation for combining the visits, we then normalize the reduced individual visit spectra and align to a reference frame. We determine velocity shifts between individual visits by cross-correlating each visit with a high signal-to-noise visit as the reference; this reference is marked in Table 1. Because of the potential to artificially broaden the combined spectra, we are very careful and strategic throughout this process. The cross-correlation is performed across the spectra by one-fourth of an order at a time with 0.1 km s^{-1} steps between the reference and the spectrum to be aligned. The observed velocity shift between the two visits then corresponds to the peak of cross-correlation function (for each one-fourth order), which is found by fitting a quadratic to the top 100 points (5 km s^{-1} on each side of the peak). The uncertainty of the peak location (i.e., velocity shift) is estimated from the fitting error found from additionally fitting a Gaussian peak. If the location of the quadratic and Gaussian peaks differ by more than 15 km s^{-1} , then the solution is thrown out. Therefore, this process also serves as a tool to exclude non-ideal CCF shapes where the peak value is less reliable. The final velocity shift is found by first taking a 1σ cut defined by the standard deviation across all measurements. Then, using the fitting errors as weights, the final velocity shift is computed by a weighted average. Each visit is then shifted to the frame of the reference visit using the measured velocity shift, and interpolated onto the same wavelength solution. Next, the flux of each visit is normalized by dividing by the median flux near 15950 Å in the *H*-band and 21920 Å in the *K*-band.

Finally, the combined spectrum is produced with a weighted average of the 10 aligned visit spectra. The weight for each visit corresponds to the uncertainties of the telluric-corrected flux at each pixel. The uncertainties of the combined spectrum are given by the standard deviation of the mean. The final combined spectrum has an average signal-to-noise ratio of ~ 640 in the *H*-band and the *K*-band. The full spectra are shown in Figures 1 and 2, including a close look of the highly resolved detail shown by zooming in on some interesting spectral features.

3. Analysis

With this work, we characterize the mean surface magnetic field of the famous young star CI Tau using the combined high-quality IGRINS spectrum. We bolster our results by providing blind, independent measurements obtained with the same IGRINS dataset; at the same time, we directly compare two distinct modeling methods to measure the magnetic field strength via the Zeeman broadening in the NIR.

3.1. Method 1: Magnetic Field Strength and Stellar Parameterization with MoogStokes

3.1.1. Model Grid

For the first method, we determine the mean magnetic field strength of CI Tau through stellar parameterization with MoogStokes (Deen 2013). The one-dimensional LTE radiative transfer code Moog (Snedden 1973) has been a staple for stellar spectral synthesis since its creation. We optimize on the familiarity and reliability of this foundation by using a customization of Moog called MoogStokes. MoogStokes synthesizes the emergent spectra of stars including magnetic effects due to a uniform radial magnetic field in the photosphere. MoogStokes calculates the Zeeman splitting of

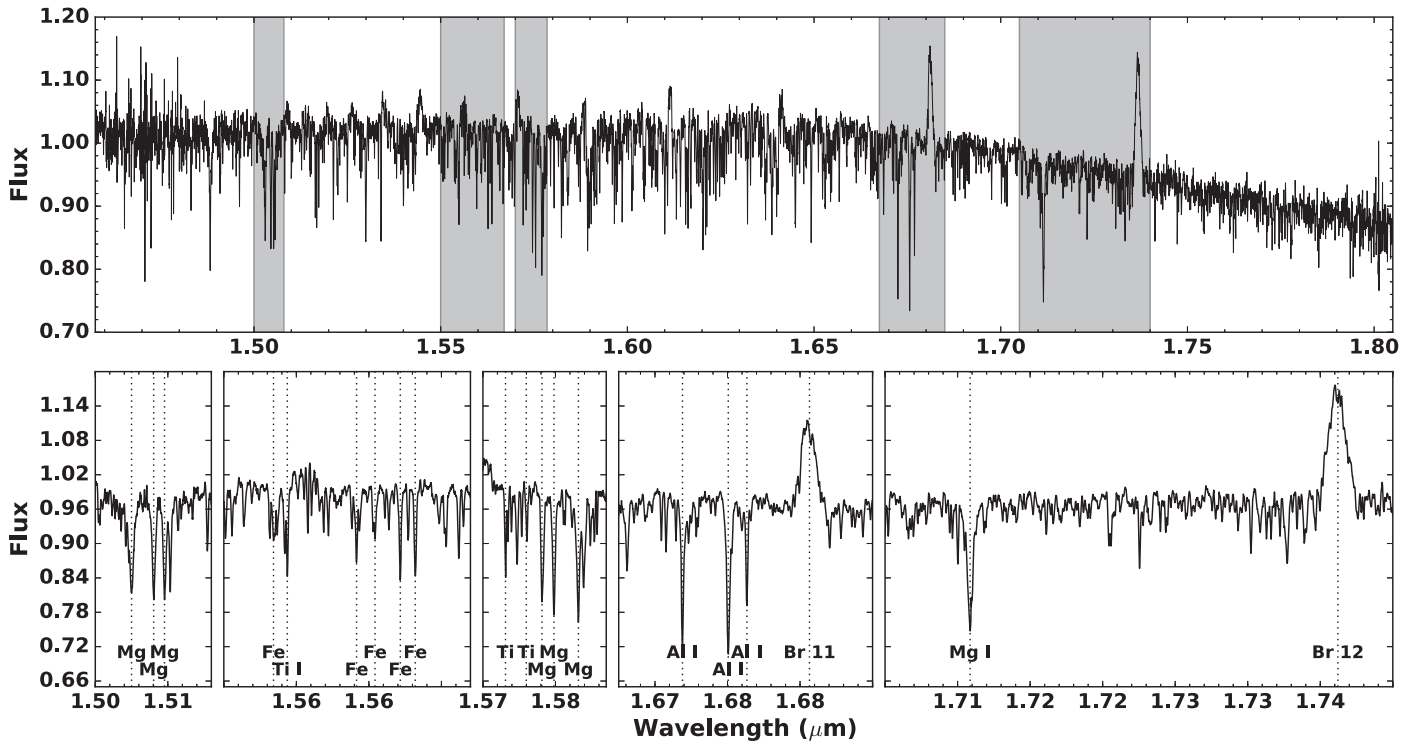


Figure 1. Views of the final combined IGRINS spectrum of CI Tau. The top panel shows the full H -band spectrum, normalized using the median flux near $1.595 \mu\text{m}$ in the H -band and $2.192 \mu\text{m}$ in the K -band. Bottom panels zoom in on regions of interest in the flattened version of the same spectrum.

(The data used to create this figure are available.)

an absorption line by using the spectroscopic terms of the upper and lower state to determine the number, wavelength shift, and polarization of components into which it will split for a given magnetic field strength. Thus, the mean magnetic field strength is one of the fundamental input parameters for MoogStokes.

MoogStokes synthetic spectra are generated using the stellar parameters of effective temperature T_{eff} , surface gravity $\log g$, and magnetic field strength B . The parameters of effective temperature T_{eff} and surface gravity $\log g$ are defined by the model atmospheres, whereas the magnetic field strength can be input as desired. The models are linearly interpolated between grid points as needed. We generate a three-dimensional grid using solar metallicity (appropriate for YSOs; Padgett 1996; Santos et al. 2008) and the MARCS model atmospheres (Gustafsson et al. 2008) resulting in grid that spans $T_{\text{eff}} = 3000\text{--}5000 \text{ K}$, $\log g = 3.0\text{--}5.0$, and $B = 0.0\text{--}4.0 \text{ kG}$. For each grid model, MoogStokes generates raw emergent spectra synthesized at seven viewing angles. It then applies the effects of limb darkening and rotational broadening to produce a disk averaged synthetic spectrum (Deen 2013). We set the rotational broadening to match that of CI Tau, which is $v \sin i = 10.0 \text{ km s}^{-1}$ (Biddle et al. 2018). Additionally, we convolve all synthetic spectra with a Gaussian kernel to simulate the $R = 45,000$ resolving power of IGRINS.

3.1.2. Identifying the Best-fit Synthetic Spectrum

To identify the mean magnetic field strength of CI Tau, we find the best-fit MoogStokes synthetic spectrum compared to the combined IGRINS spectrum of CI Tau. We follow a method similar to that of Sokal et al. (2018). First, further processing of the combined spectrum is required to compare

to the MoogStokes models. We stitch the orders of the observed CI Tau spectrum together and flatten using an interactive Python script (based on <http://python4esac.github.io/plotting/specnorm.html>). The continuum estimation and flattening process likely contributes one of the greatest sources of uncertainty to the fitting process, and is propagated into estimating the uncertainties (which is discussed later on).

Throughout the fitting procedure to identify the best-fit MoogStokes' synthetic spectral model, we cycle between the stellar parameters (effective temperature, surface gravity, and mean magnetic field) and repeat the process until convergence is reached. For the stellar parameter being investigated, we vary the input value while setting the other two parameters to a constant value. We evaluate the goodness-of-fit across the grid space (e.g., Cushing et al. 2008). We then adopt this new best value before iterating with the other parameters. The goodness-of-fit is tested over parameter sensitive spectral regions that are similar to Doppmann & Jaffe (2003), Yang et al. (2005), Sokal et al. (2018). The effective temperature is evaluated using the Sc and Si lines in the Na interval ($2.202\text{--}2.212 \mu\text{m}$), the surface gravity with the $(2\text{--}0) \text{ }^{12}\text{CO}$ interval ($2.2925\text{--}2.3022 \mu\text{m}$), and the mean magnetic field strength with the TiI lines at 2.221 , 2.223 , 2.227 , and $2.231 \mu\text{m}$.

To begin the fitting process, we start with an initial model based on the literature: effective temperature of $T_{\text{eff}} = 4050 \text{ K}$ ($\log T_{\text{eff}} = 3.6085$; Andrews et al. 2013; McClure et al. 2013), surface gravity $\log g = 3.85$ extrapolated from CI Tau's stellar mass and age ($M_* = 0.8 M_{\odot}$ at 2 Myr ; Guilloteau et al. 2014) using the Baraffe et al. (1998) models, and a by-eye estimate for the magnetic field strength of $B = 2.0 \text{ kG}$. The veiling is measured at $2.2 \mu\text{m}$ for each synthetic model using a least

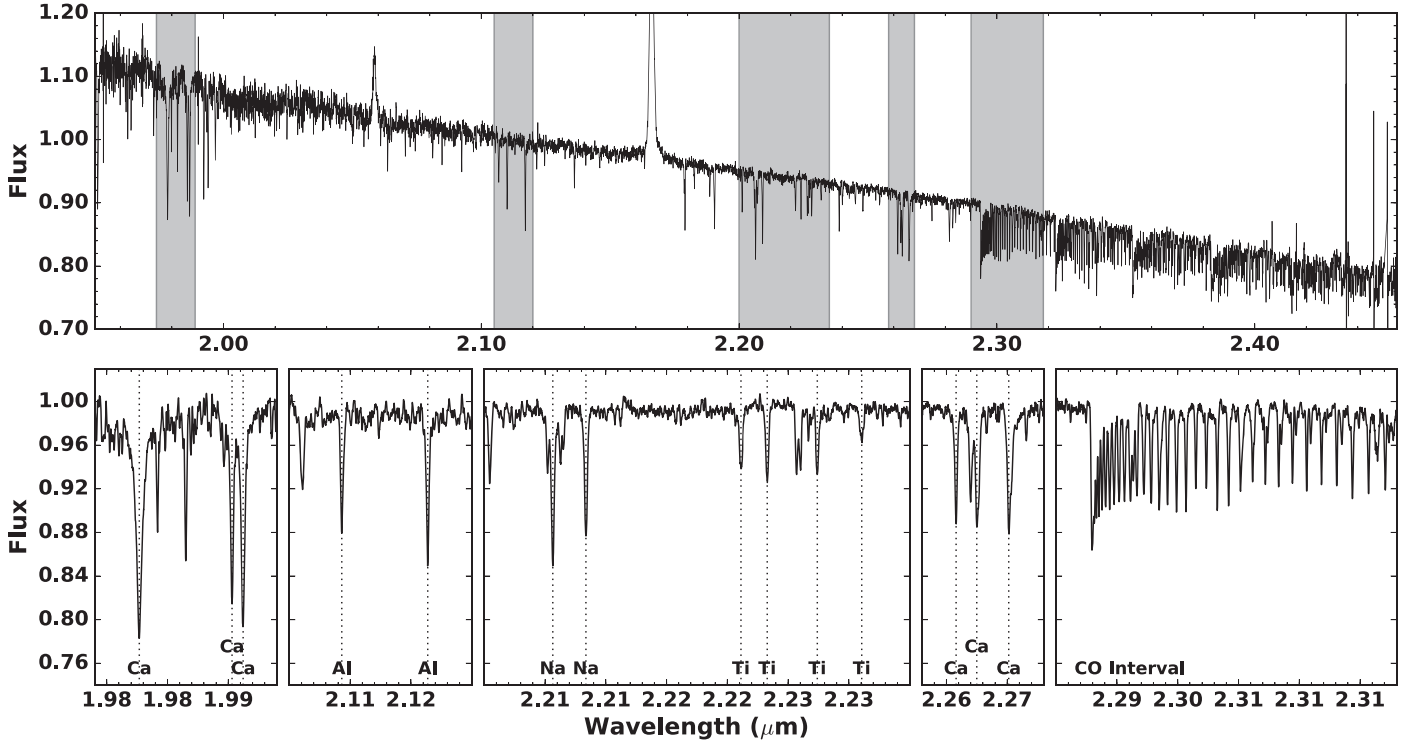


Figure 2. Same as Figure 1 showing the *K*-band spectrum of CI Tau. The full *K*-band spectrum is normalized using the median flux near $2.192 \mu\text{m}$. (The data used to create this figure are available.)

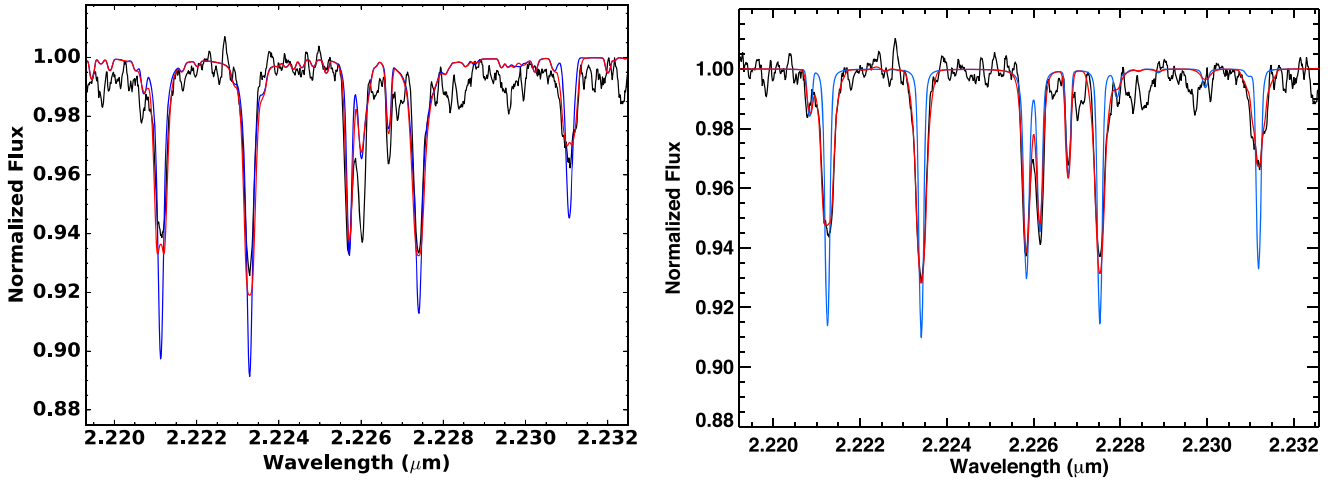


Figure 3. A comparison of the results of our two methods to measure the mean magnetic field, illustrated by the best-fit models (with and without the magnetic field contribution) in comparison to the Ti I interval of combined IGRINS spectrum of CI Tau. Both methods roughly agree, obtaining a value of $\sim 2.2\text{--}2.3 \text{ kG}$, despite different interpretations of the continuum level and method. Left: method 1/MoogStokes. Right: method 2/ SYNTHMAG. Red shows the best-fit model corresponding to a mean magnetic field of $B = 2.2\text{--}2.3 \text{ kG}$ and the blue line shows the same model, including the same veiling, with the magnetic effects turned off ($B = 0.0 \text{ kG}$).

squares fitting routine to the observed spectrum. The models are artificially veiled using the measured value and a warm dust spectrum corresponding to a $\sim 1500 \text{ K}$ blackbody.

We find the best-fit MoogStokes synthetic spectral model to the combined IGRINS spectrum of CI Tau corresponds to the stellar parameters of $T_{\text{eff}} = 4025 \pm 25 \text{ K}$, $\log g = 3.9 \pm 0.05$, and $B = 2.15 \pm 0.15 \text{ kG}$ with a veiling of $r_k = 2.3$, and plot this comparison in Figure 3. Uncertainties on the best-fit values of the stellar parameters are estimated by performing a Monte Carlo (MC) simulation, and represent uncertainties in the

fitting. We construct simulated observed spectra that are randomly sampled at each pixel from a Gaussian distribution centered on the combined IGRINS flux and with a width based on the uncertainty. We estimate a contribution of an additional 0.5% uncertainty to propagate the uncertainties due to the flattening process into the error on our fitting, and add it in quadrature to the existing uncertainties.

We ran the MC simulation and fitting routine 1000 times. The best-fitting synthetic spectrum for each randomly sampled observed spectrum is found by minimizing the goodness-of-fit

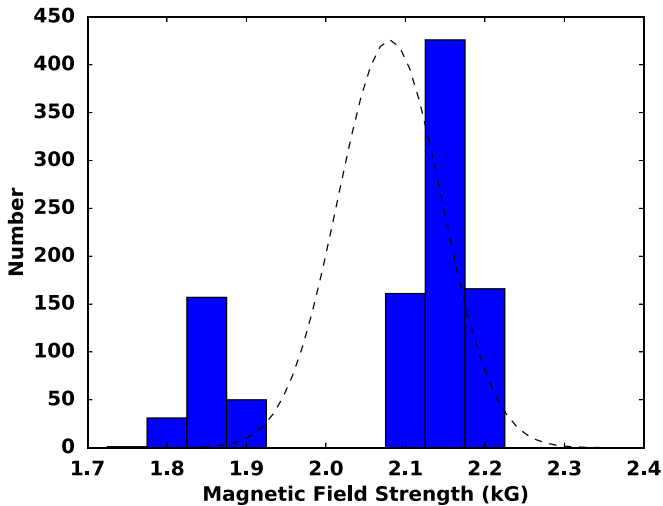


Figure 4. The distribution of the magnetic field strength values found while running a Monte Carlo simulation, during which all stellar parameters were allowed to vary, to estimate the uncertainties across the entire parameter space. The final best-fit value of the mean magnetic field strength of 2.15 kG corresponds to the peak, mode, and median of this distribution of the best MC fit values when binned every 0.05 kG, as shown. The Gaussian fit to the distribution is plotted with a dashed line, and the standard deviation gives the adopted uncertainty of ~ 0.15 kG in the mean field strength measurement. The distribution is clearly bimodal, which is likely due to different features of the line profiles dominating in the different Monte Carlo runs and may suggest that a multi-component magnetic field is more realistic.

statistic. We automate the same iterative process as with determining the best-fit model, except that the value of the veiling is held constant to the best-fit value of $r_k = 2.3$. The standard deviation of the distributions of the best-fit MC values for the stellar parameters of effective temperature and surface gravity matched the model grid spacing (25 K and 0.05, respectively). The distribution for the best-fit MC values of the magnetic field strength is highly bimodal with the two peaks corresponding to ~ 1.85 and 2.15 kG, as shown in Figure 4. The mean magnetic field strength of the best-fit model corresponds to the peak, mode, and median of this histogram of the best MC fit values. The adopted uncertainty of 0.15 kG is reflective of the standard deviation of the full distribution, which was derived by allowing the stellar parameters to vary in the MC simulation. This bimodality is suggestive of a multi-component magnetic field, which is discussed further in Section 4.1.

3.2. Method 2: Magnetic Field Modeling with SYNTHMAG

One of the goals of this study is to perform a magnetic analysis on CI Tau using two independent methods that have been used for magnetic analysis of young stars. The analysis done in this section was performed blindly and is thus independent of knowledge of the results obtained in the last section. A number of studies (e.g., Johns-Krull et al. 2004; Yang et al. 2005, 2008; Johns-Krull et al. 2009; Yang & Johns-Krull 2011) have analyzed *K*-band spectra of young stars to measure the distribution of magnetic field strengths on the stellar surface, as well as to measure the mean magnetic field strength using the SYNTHMAG code (Piskunov 1999). These studies have generally followed the procedures outlined in Johns-Krull et al. (1999) and Johns-Krull (2007). We follow these same procedures here. As such, the method here and the MoogStokes method outlined in Section 3.1 strictly followed

their respective methodology. We note that the impact of any difference within the processes could be worthy of its own investigation, but is beyond the scope of this project. Briefly, these previous studies utilizing *K*-band spectra with similar spectral resolution to IGRINS have found that the best fits to the broadening observed in the Ti I lines result when a distribution of magnetic field strengths is allowed on the stellar surface. However, because of the finite spectral resolution and the intrinsic width of the photospheric line profiles, even in the absence of a magnetic field (e.g., due to thermal, turbulent, and rotational broadening), only a limited number of different magnetic field components are allowed when fitting the observed spectra. It has been found that a 2 kG resolution in the field results in fairly robust fits. Meanwhile, significantly finer resolution in the allowed magnetic field strengths results in magnetic field distributions that oscillate fairly substantially, due to degeneracies associated with trying to constrain field components that vary in strength by a relatively small amount. Therefore, we fit model spectra to the observed spectra of CI Tau by allowing field strengths of 0, 2, 4, and 6 kG and we solve for the filling factor of each of these field components.

As noted earlier, the *K*-band contains several magnetically sensitive Ti I lines in addition to a number of relatively magnetically insensitive lines such as the CO lines of the $v = 2-0$ rovibrational transitions near $2.3 \mu\text{m}$. Historically, for magnetic field analysis we have used the four strong Ti I lines between 2.220 and $2.232 \mu\text{m}$ due to the small wavelength grasp of earlier high resolution IR spectrometers, such as CSHELL (Tokunaga et al. 1990; Greene et al. 1993) on the NASA IRTF. IGRINS contains all four of these lines in a single order so they are recorded simultaneously. Between the two pairs of Ti I lines are four fairly strong lines of Fe I, Sc I, and Ca I. We include these lines in the analysis here, taking their line data from the VALD atomic line database (Kupka et al. 1999) and computing their Zeeman splitting patterns from the transition data contained in the database. These lines have smaller Landé- g values than the nearby Ti I lines, but they are non-zero and are useful for magnetic analysis.

To fit the observed spectrum of CI Tau, we compute model spectra with SYNTHMAG covering the wavelength range $2.219-2.233 \mu\text{m}$ and $2.309-2.316 \mu\text{m}$ (wavelengths given in air). The first region contains the magnetically sensitive atomic lines of Ti I and the less sensitive Fe I, Sc I, and Ca I lines. The second region contains ~ 10 CO lines, which have very little magnetic sensitivity and serve as a check on other line broadening mechanisms such as rotation and macroturbulence. Basic atmospheric parameters are required to perform the spectrum synthesis, so we took estimates of these from the analysis of McClure et al. (2013) who give $T_{\text{eff}} = 4060$ K, $R_* = 1.41 R_\odot$, and $M_* = 0.80 M_\odot$. This mass and radius corresponds to a gravity of $\log g = 4.04$. Since this analysis was done independent of the MoogStokes analysis, we selected the stellar parameters without knowledge of the results of the previous section. We use the “next generation” (NextGen) model atmospheres (Allard & Hauschildt 1995) to compute the synthetic spectra. These model atmospheres are tabulated on a regular grid of effective temperature, gravity, and metallicity. We assume solar metallicity for CI Tau and choose the NextGen model from the grid that most closely matches the stellar parameters from McClure et al. (2013). Specifically, we take $T_{\text{eff}} = 4000$ K and $\log g = 4.0$. We assume a micro-turbulent broadening of 1 km s^{-1} and a radial-tangential

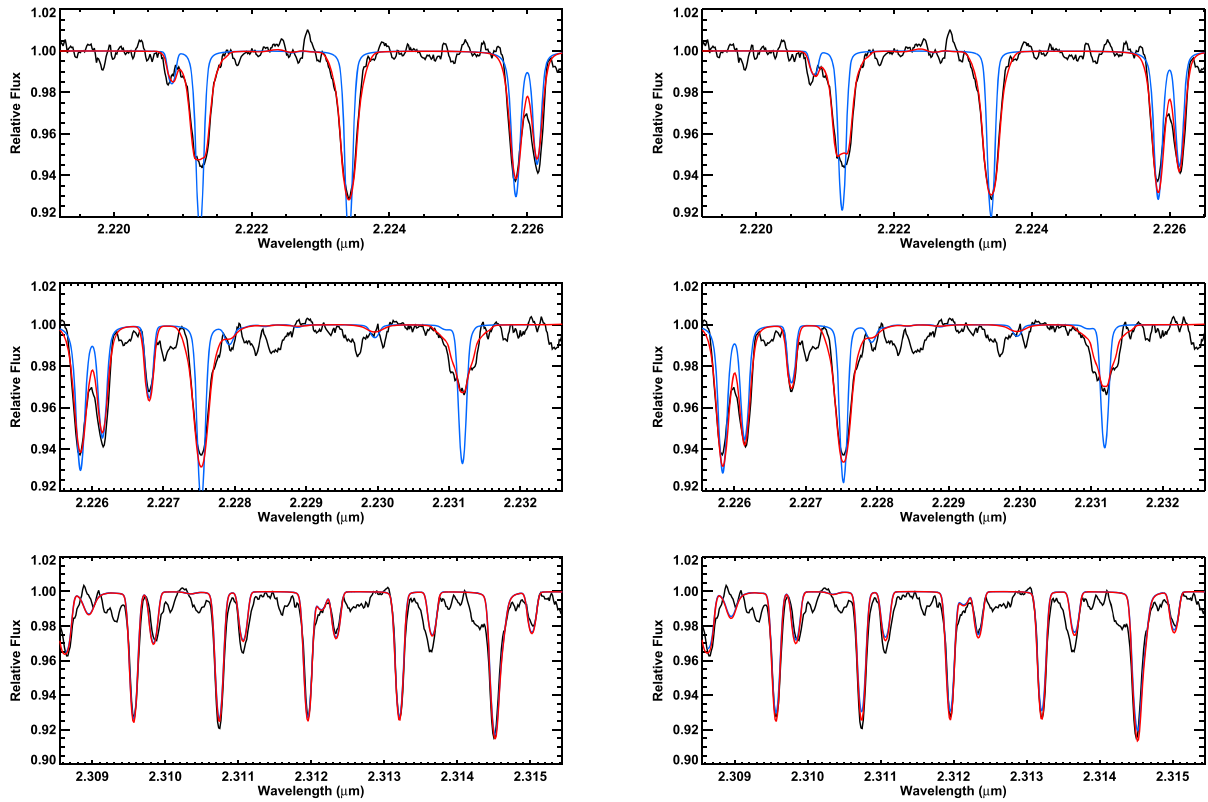


Figure 5. The results of fitting SYNTHMAG model composed of a distribution of field strengths to the observed CI Tau spectrum. The IGRINS observations are shown in black in both panels. In the left-hand set of panels, the $T_{\text{eff}} = 4000$ K model with no magnetic field is shown in cyan, and the model with the magnetic field filling factors for the $T_{\text{eff}} = 4000$ K model from Table 2 is shown in red. The two top panels show the detail for the magnetically sensitive Ti I lines while the bottom panel shows the magnetically insensitive CO lines. Note how narrow the CO lines are and how broad the Ti I lines are, which is indicative of a strong magnetic field. The right-hand panels show the same thing but with the $T_{\text{eff}} = 4200$ K models.

Table 2
Composite Field Fits

Assumed T_{eff}	Filling Factor 0 kG Field	Filling Factor 2 kG Field	Filling Factor 4 kG Field	Filling Factor 6 kG Field	ΣBf (kG)	Veiling
4000	0.21	0.54	0.17	0.08	2.26 ± 0.06	2.01 ± 0.05
4200	0.19	0.56	0.16	0.09	2.30 ± 0.06	1.83 ± 0.05

macroturbulence of 2.0 km s^{-1} . Values for both types of turbulence are appropriate for a star with CI Tau’s parameters (Gray 2005); however, our results are quite insensitive to the specific values of micro- and macroturbulence because other line broadening mechanisms (rotation and magnetic) dominate. The last thing needed to compute the synthetic spectra is the stellar $v \sin i$, which we take to be 10.1 km s^{-1} from Biddle et al. (2018). We remind the reader that this analysis was performed independently from Section 3.1, and therefore the inputs may vary.

As mentioned earlier, we assume regions on the stellar surface with field strengths of 0, 2, 4, and 6 kG. We compute models for each field strength using SYNTHMAG, assuming that the field is oriented radially at the stellar surface, which is generally motivated by solar observations. In the solar case, it is also known that the regions of highest photospheric magnetic field are in dark, cool sunspots. However, we do not know the general relationship between field strength and temperature for other stars. We therefore assume that each field region has the same temperature (4000 K). To compute the final profile, we then add the spectra together according to the assigned filling factor (f_i) for each component. We also add in veiling from the

disk emission in the two regions of spectra we are fitting. While these regions are close in wavelength, it is possible the veiling could be somewhat different between the two, so we allow the veiling in each region to be a free parameter. Finally, we convolve the resulting profile with a Gaussian to represent the instrumental line broadening with an assumed spectral resolving power of $R = 45,000$ to match that of IGRINS. Our model then has five free parameters: filling factors (f_2 , f_4 , and f_6) for the 2, 4, and 6 kG field regions (f_0 is set by the requirement that the filling factors sum to 1.0), and the veiling in the two spectral regions. It is important to note that the only free parameter in the CO region is the veiling in this region—all of the other parameters that affect the line strength and width of the CO lines are fixed because they have negligible magnetic sensitivity. We use the nonlinear least squares technique of Marquardt (see Bevington & Robinson 1992) to fit the observed spectrum by minimizing χ^2 over the regions shown in Figure 5, determining the best-fit parameters that are given in Table 2. Before comparing the model to the observed spectrum, we normalize the regions of interest in the observed spectrum by dividing out a second-order polynomial fit over a small spectral window. Furthermore, this fitting procedure is

performed on individual orders without requiring any merging. The fitted spectral regions and best-fit final synthetic spectrum are shown in the left-hand panel of Figure 5. The veiling in the two regions is found to be the same within the uncertainties (see next paragraph), so we only report the mean of the two veilings. The sum of the field strengths and their respective filling factors (ΣBf) represents the mean field on the surface of CI Tau, and we find this value to be 2.26 ± 0.06 kG. We also plot the best-fitting spectrum from this procedure in Figure 3 for comparison with the results from the MoogStokes analysis.

To estimate uncertainties on our fitted field parameters, we again turn to Monte Carlo simulation. The data reduction process returns uncertainties in the observed spectrum; however, the observed scatter of the observations around the best-fitting model is larger than these estimated uncertainties. To provide more realistic values, we compute the standard deviation (0.0052) of the residuals of the observed spectrum with the fit subtracted out and add this in quadrature to the uncertainties returned by the data reduction procedure to get final observational uncertainties. We then create a new *observed* spectrum by adding Gaussian random noise with an amplitude given by this revised observational uncertainty to original observation, and we analyze this spectrum in the same manner as the original data. We repeat this process 1000 times and take the standard deviation of the resulting values as the uncertainty in the fitted quantities, which we report in Table 2. For any given fit, the filling factor of the different field components can trade off each other somewhat, so they have larger individual uncertainties which are correlated; however, the mean field is better determined so we only report the uncertainty of this quantity and the veiling in Table 2.

While the fit in Figure 5 does a good job of fitting the Ti I lines, the fit to the Fe I and Sc I lines at $2.226 \mu\text{m}$ is not quite as good, possibly indicating the atmospheric parameters (e.g., T_{eff} or $\log g$) are not optimally chosen. Therefore, we repeated the same analysis but using a NextGen model with $T_{\text{eff}} = 4200$ K and $\log g = 4.0$. This also gives us a chance to see how sensitive our magnetic results are to an error in the assumed effective temperature. The results of this analysis are also reported in Table 2, where it can be seen that we determine a mean field of 2.30 ± 0.06 kG for CI Tau, a value well within 1σ of our estimated uncertainty. This good agreement is likely because we are detecting actual Zeeman broadening in the Ti I lines, giving us a very good handle on the magnetic field properties of this CTTS. The best-fit model from this fit is shown in the right-hand panel of Figure 5. This model fits the lines at $2.226 \mu\text{m}$ somewhat better, but does not fit the Ti I lines quite as well, which probably indicates that the best temperature for CI Tau is between 4000 and 4200 K, this result is not surprising based on previous studies, the potential for an inhomogeneous photosphere, and our earlier analysis.

4. Discussion

4.1. A Comparison of Methods

A comparison of the results of the blind analysis by our two methods shows good agreement. Both independent methods find the value of the mean magnetic field of CI Tau is $B \sim 2.2$ kG. The resulting best-fitting synthetic spectra are shown in Figure 3, both with the derived magnetic field and also without any magnetic effects included. Such agreement is not entirely surprising because the important physics for this

result is the same as the agreement between different temperature inputs in the SYNTHMAG analysis: the Zeeman broadening of the Ti I lines is caused by a strong magnetic field. The SYNTHMAG method produces a somewhat better fit, which is not surprising because it is fitting multiple magnetic components. Given that the MoogStokes method adopted the goodness-of-fit metric while SYNTHMAG instead adopted χ^2 , and a direct comparison of goodness-of-fit between the two methods is complicated by the size of the spectral window used in the respective fits, we can narrow down on the region around the Ti I lines to get an estimate of the difference in the two methods for fitting the magnetic signatures contained in the data. By computing χ^2 for the spectral regions shown in 3, we find that the SYNTHMAG fitting results in a factor of 2.7 improvement in χ^2 relative to MoogStokes.

Moreover, we find that the agreement of our results suggests that measuring the actual Zeeman broadening is quite reliable for estimating the mean magnetic field of the photosphere. The agreement of Zeeman broadening measurements using different models has also been found previously. However, this agreement was specifically tested here. The list of the differences between the MoogStokes and SYNTHMAG methods is long, some details that vary are: the assumed continuum in the observed data, the stellar atmosphere used in the code, and even the composition of the magnetic field (i.e., a uniform radial field in the MoogStokes method versus a composite field with the SYNTHMAG method). These fundamental differences in the treatment of the field are similar in nature to the tests performed by Shulyak et al. (2014), who explored two different assumptions regarding the field geometry in their analysis of Zeeman broadening measurements in active M dwarfs and found very good agreement in the mean field strengths determined under the different assumptions. Thus, it is likely that measurements utilizing magnetic broadening are even less sensitive to some of the input parameters, as is perhaps expected, at least for strong fields such as in CI Tau. For instance, the continuum value was of great concern in both blind analysis runs—leading to additional uncertainty being added in the Monte Carlo simulation for propagating this effect into the MoogStokes method results—and yet the outcome produced very similar measured values, regardless of different continuum definitions.

While both methods are successful, relying on essentially the same physics to get at the measurement of the mean magnetic field despite a multitude of differences, the different approaches of the two methods are also their strengths, and are also the reason why both are interesting to consider and use. MoogStokes, identifies the mean magnetic field strength along with the effective temperature and surface gravity. Thus, this measurement is part of the full picture—the magnetic field strength does not rely on an assumed characterization. Alternatively, the SYNTHMAG analysis employed here fits a multi-component magnetic field that is much more realistic. It identifies not only the mean field strength but also the filling factors associated with different field components. The MoogStokes fitting results for CI Tau may also indicate that a single magnetic field strength is not the best description. In particular, the MC error estimation results in a bimodal distribution for the mean magnetic field strength (Figure 4). We suspect that this is a result of either the broadening in the wings or the more narrow core dominating the fitting process, with the variation between the two resulting from the MC

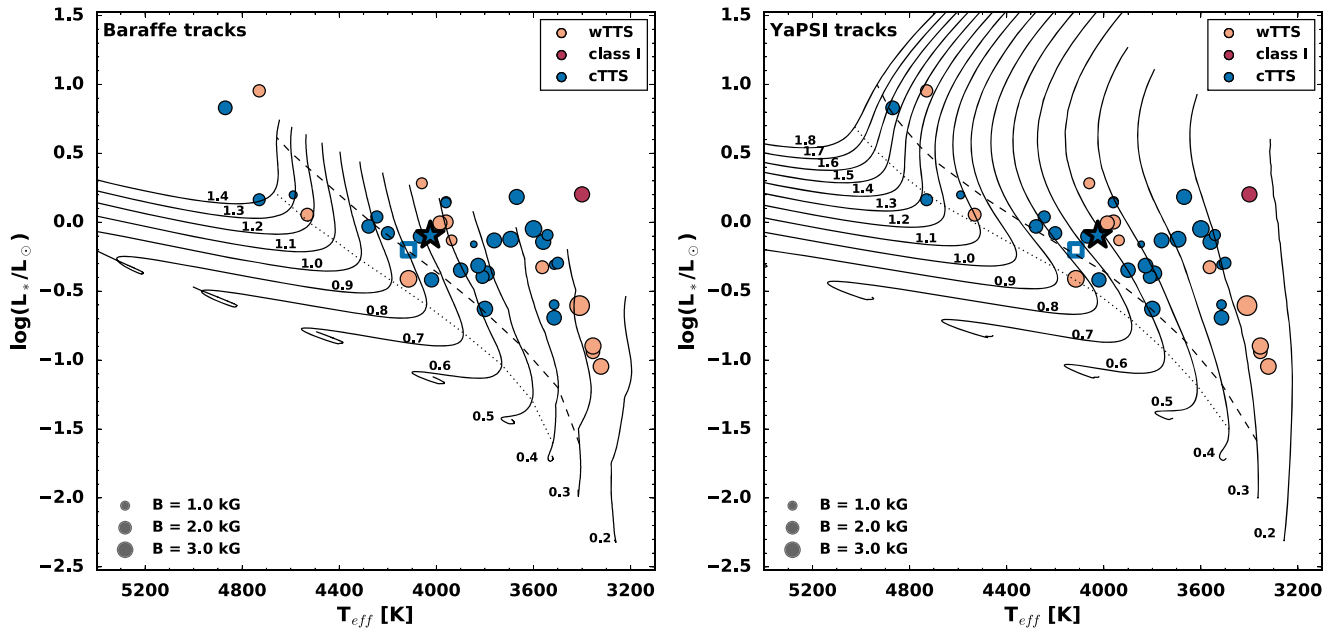


Figure 6. CI Tau (as a star symbol) placed in the HR diagram among an updated sample of TTSs (circle symbols) for which the surface magnetic field strength is measured from observations of Zeeman broadening. Details and references for the comparison sample are given in Table 3. The evolutionary tracks of Baraffe et al. (2015), Spada et al. (2017) are plotted with solid-black lines and labeled with the model’s stellar mass in Solar masses. The locations on each track at which a radiative core starts forming and the mass of the radiative core is 0.4 the stellar mass are indicated by dashed and dotted lines, respectively. The size of the symbols corresponds to the strength of the magnetic field. The color of the symbols corresponds to the type of TTS. The square symbol marks GM Aur, which we will use as a reference later.

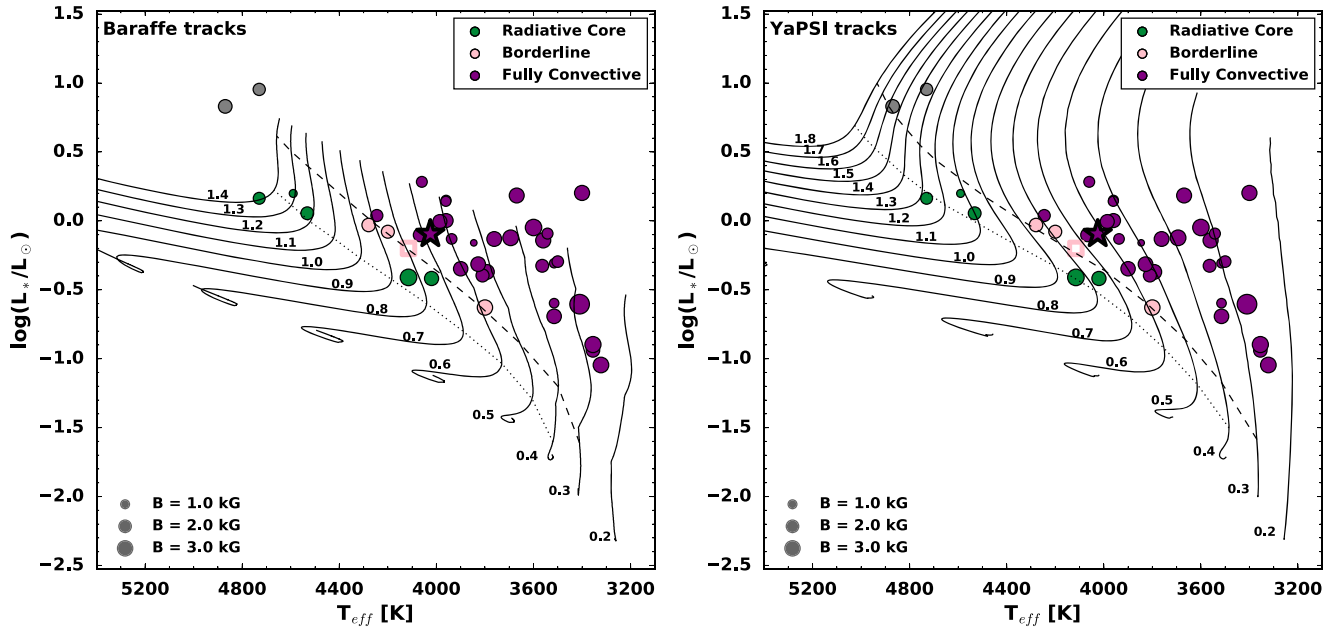


Figure 7. Additional versions of the HR diagram are shown in Figure 6, comparing the evolutionary tracks of Baraffe et al. (2015) and Spada et al. (2017) in the left-hand and right-hand panels, respectively. Evolutionary tracks are plotted with solid-black lines; and the dashed lines indicate the formation of a radiative core and where the mass of the radiative core is 0.4 the stellar mass. In both panels, the color of the symbols corresponds to the approximate stellar structure of each source. The star symbol marks the location of CI Tau. The square marks GM Aur, which we will use as a reference later in the paper.

sampling. Thus, the values of the two peaks in this distribution hint that a zero or weak component is an important contribution to the overall field, where this contribution is specifically taken into account in the SYNTHMAG analysis (Table 2).

4.2. CI Tau Among Other Magnetic TTSs

We put our results into context by placing CI Tau in the HR diagram in Figures 6 and 7. In addition, we directly plot the

strength of the magnetic field versus the predictions of the field strength derived from equipartition arguments (Figure 8), as well as versus the effective temperature (Figure 9). For comparison, we choose a compilation of TTSs for which the magnetic field strength has been measured through the observed Zeeman broadening; electing for a sample of similar measurements for consistency. This comparison sample includes specific studies of TTSs from Taurus (Johns-Krull 2007), TW

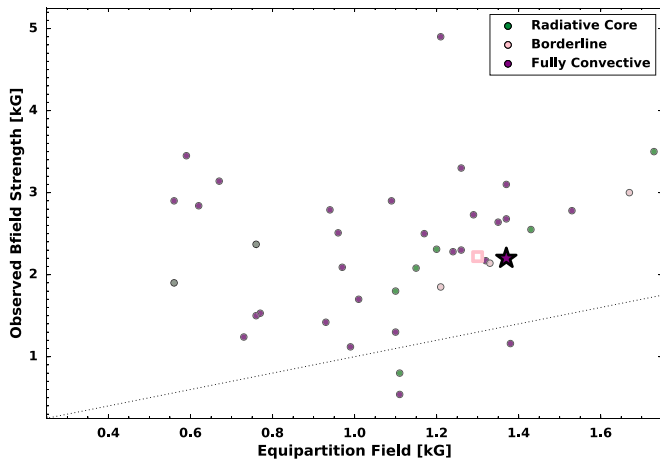


Figure 8. The measured mean magnetic field vs. the magnetic field predicted by pressure equipartition in the photosphere for the stars in Table 3. The dashed line shows the line of equality. The vast majority of the stars lie above this line, which indicates that their photospheres are magnetically dominated. In addition, no correlation with the predicted equipartition field exists.

Hydra (Yang et al. 2008), and Orion (Yang & Johns-Krull 2011) regions, as well as a group of (low to) intermediate TTSs from Lavail et al. (2017). Consequently, these stars, which are all TTSs, have different ages spanning this young evolutionary phase, and therefore make an excellent test group. To yield a more accurate comparison, we update the stellar parameters of the sample to current literature values whenever possible (see Table 3 for the values and references). Effective temperatures of the TTSs in Taurus and TW Hya are estimated from the spectral typing of Luhman et al. (2017) using the conversion of Herczeg & Hillenbrand (2014); effective temperatures of the Orion TTSs are drawn from the IN-SYNC survey using APOGEE (Da Rio et al. 2016). Notably, we correct the stellar luminosities to the current *Gaia* distance (Bailer-Jones et al. 2018). At the same time, it is important to remember that the magnetic field measurements based on the Zeeman broadening are fairly insensitive to other stellar parameters, such as effective temperature. All values are presented in Table 3.

It is apparent that CI Tau fits in well with the rest of the observed sample of TTSs in the HR diagram. CI Tau falls on the vertical Hayashi track, as depicted by the overlaid Baraffe and Yale-Potsdam Stellar Isocrones (YaPSI) evolutionary models (Figure 7 in Baraffe et al. 2015; Spada et al. 2017), and is in a grouping of other similar stars. As the size of the symbols indicates, the stars in this grouping all have similar magnetic field strengths. The HR diagram shown in Figure 6 is color-coded by TTS type; and the subset of stars near CI Tau include both wTTS and cTTS. In Figure 7, we plot additional HR diagrams to show the evolutionary tracks of Baraffe et al. (2015) and Spada et al. (2017), and we color code corresponding to the approximate internal structure of the source. In all of the shown HR diagrams, the dashed line indicates the formation of a radiation core, and a dotted line corresponds to where the radiative core contains 40% of the stellar mass, for the evolutionary tracks being used. CI Tau is clearly above these boundaries and thus likely fully convective.

Considering the importance of the magnetic field to TTSs and potential planetary systems, it is also worthwhile to examine the observed magnetic field strengths because there is much to be learned regarding the origin and regulating mechanisms of the field. An early guiding principle for

understanding the magnetic field measurements of cool stars was that the field strength was set by pressure equipartition with the surrounding photosphere. For active main-sequence stars, it was found that the measured fields correlated very well with the equipartition values, and it was also found that the maximum value of the measured field strength equaled the equipartition values to within $\sim 15\%$ (Saar 1991, 1994). In Figure 8, we plot the measured mean field of our TTS sample versus the field predicted by pressure equipartition in the photosphere. We determine the equipartition field strength by taking the pressure, P_{eq} , in the NextGen model atmospheres (Allard & Hauschildt 1995) at the level where the local temperature is equal to the effective temperature for the appropriate effective temperature and gravity of each star. We then set $P_{\text{eq}} = B_{\text{eq}}^2/8\pi$ and solve for the equipartition field, B_{eq} . This represents the maximum field strength that can be confined by the gas pressure in the surrounding non-magnetic atmosphere. Figure 8 shows no correlation between the measured fields and the predicted fields, with a Spearman rank-order correlation coefficient (Zwillinger & Kokoska 2000) of 0.20 with an associated false alarm probability of 0.22. In addition, the vast majority of the measured fields are well above the equipartition values, with the median ratio of the observed to equipartition field equal to 1.9. This suggests that for most TTSs, the entire surface is covered in magnetic field and, therefore, the field strength is not set by pressure equipartition in the visible photosphere. Similar conclusions were found by Johns-Krull (2007).

While equipartition does not appear to be operating in this sample, we have found that plotting the mean magnetic field strength versus the effective temperature produces an intriguing result. As shown in Figure 9, a trend is apparent in that many of the TTSs appear to lie in a region roughly following a negatively sloped line across the B versus T_{eff} space. This trend is suggestive and may be indicative of an evolutionary change leading to a pileup in this plot. We find no obvious distinction in the sample according to the type of star (classical or weak-lined TTS). However, color coding the sample by their stellar structure as defined by their respective placement in the HR diagram (Figure 6) may suggest that this trend is related to the evolution and internal structure. We see that the stars that have formed a radiative core lie above and to the right of the trend defined by the apparent pileup in this plot.

Ultimately more data is needed to rigorously test if there is a true pileup observed in this mean magnetic field strength versus effective temperature plot; however, we present an exploratory examination. Statistically, we would not expect a strong correlation coefficient for the entire sample because only the pileup sources display a by-eye trend. Therefore it is preferable to test the subset of pileup sources. However, identifying this subset can be subjective, especially because not all viewers may even see a pileup. The presence of a true pileup suggests that some fraction of the points in Figure 9 cluster closely to define a trend. Therefore, we apply a clustering algorithm to provide an easy and reproducible method of identifying a majority of the pileup group. The effective temperatures and mean magnetic field strength values are first standardized by removing the mean and scaling to unit variance, as is best practice for applying most clustering algorithms. We use Density-Based Spatial Clustering of Applications with Noise (DBSCAN; Ester et al. 1996) from Python’s scikit-learn package (Pedregosa et al. 2011) because it has the specific advantage of being based on density. DBSCAN

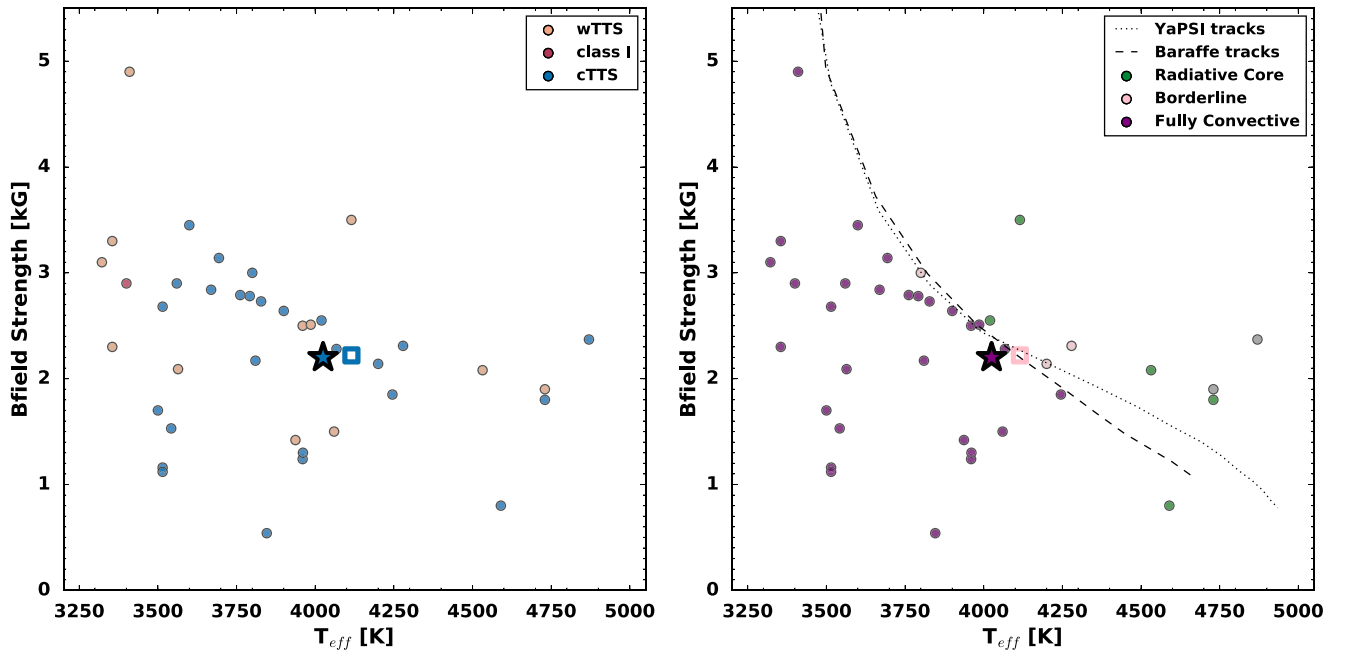


Figure 9. A plot of the mean magnetic field strength vs. the effective temperature for CI Tau and a comparative sample of TTSs. The colors are taken from Figure 7. A build up of sources is evident near the location of CI Tau (star symbol), roughly following a line with a negative slope. This trend may be indicative of an evolutionary change, whether it is the conversion to a dynamo from a primordial magnetic field or is explained by invoking the convective boundary. In the case of stellar structure as the origin, we can estimate a scaling relation for the maximum magnetic field strength of an equipartition field for convective instability. By inputting the stellar parameters of the Baraffe et al. (2015) and Spada et al. (2017) evolutionary tracks, we plot the maximum magnetic field strength of an equipartition field at the convective boundary (dashed and dotted lines, respectively). This relationship is evaluated at the convective boundary by scaling to the reference TTS GM Aur. Exceptional agreement is shown between the observed data, the inferred stellar structures from the HR diagram, and the predicted boundary shape.

can identify any number of arbitrarily sized and shaped data clusters. For the two parameters that define the density, we adopt the default value of 0.5 for the maximum distance to consider two sources to be related, called *eps*, and set the minimum number of sources to comprise a group to be 20% of our sample (eight sources). Reducing the minimum number of sources will result in more, smaller clusters, while increasing the minimum number of sources >8 (and the maximum distance constraint the same) does not lead to any identified clusters in this case. Fitting a DBSCAN model with these inputs results in the identification of one cluster, with the rest of the sources labeled as noise. We find that the identified cluster is an excellent match to the trend that is seen by eye and it contains the majority of the sources that match our by-eye pileup (see Figure 10).

Now that we have identified the potential pileup cluster, we can evaluate the correlation coefficient to better understand the significance of any trend between the effective temperature and mean magnetic field strength. We again use the Spearman rank-order correlation coefficient (Zwillinger & Kokoska 2000) to test for a relationship between two datasets. We use a rank-order correlation coefficient because it is designed to test for correlation without assuming any specific underlying functional form for a relationship. As would be expected, the Spearman correlation coefficient ρ is somewhat inconclusive when measured using the entire dataset, with $\rho = -0.33$ and with an associated false alarm probability of 0.035. However, the Spearman correlation coefficient for the pileup cluster identified in Figure 10 is $\rho = -0.82$ with an associated false alarm probability of 1.7×10^{-4} . A value of ± 1 would imply an exact monotonic relationship, and therefore the measured $\rho = -0.82$ is quite strong. This suggests that the effective temperature and mean magnetic field strength are correlated for the pileup group.

To try to understand any potential physics involved in the pileup, we can forge a relationship for the magnetic field strength at the fully convective boundary in this parameter space by invoking the general idea of the equipartition field, where the magnetic field pressure is balanced by the thermal gas pressure. Alternatively, Christensen et al. (2009) discovered that the magnetic field strength of planets and fully convective stars is set by the energy flux. The magnetic pressure is very similar to the magnetic energy density. For this work, we instead investigate a field that represents the maximum field that can be contained by the thermal gas pressure and evaluate it at the convective boundary by scaling to a reference star. We begin with the ideal gas law such that thermal pressure is given by $P_{th} V = N k_B T$ and substitute in for the volume $V = \frac{4}{3} \pi R^3$ and the number of gas molecules $N = \frac{M}{m_p}$. The terms are defined as follows: P_{th} is the thermal pressure, T is the temperature, k_B is the Boltzmann constant, M is the mass of the star, and m_p is the mass of a proton. Then, assuming a thermal gas profile such that $P_{th} = \frac{3 k_B}{4 \pi m_p R^3} M T$, we set the thermal pressure equal to the magnetic field pressure of $P_{mag} = \frac{B^2}{8\pi}$. While the relations and substitutions made above are fairly simplistic, we use them only to find basic scaling predictions. This results in the following maximum magnetic field:

$$\frac{6 k_B}{m_p} \times \frac{M}{R^3} \times T = B_{max}^2$$

$$B_{max} < \left(\frac{\frac{M}{M_*}}{\left(\frac{R}{R_*} \right)^3} \frac{T}{T_*} \right)^{1/2} \quad (1)$$

Table 3
Compilation of Literature Comparisons of T Tauri Stars

Source	T_{eff} (K)	$\log L/L_{\odot}$ (literature)	$\log L/L_{\odot}$ (corrected)	Distance ^a (pc)	B (kG)	Type	References ^c (T_{eff}, L, B)
AA Tau	3792	-0.35	-0.371	136.7	2.78	cTTS	Luh17+HH14,HH14,JK07
BP Tau	3810	-0.38	-0.396	128.6	2.17	cTTS	Luh17+HH14,HH14,JK07
CI Tau	4025	-0.2	-0.095	158.0	2.2	cTTS	this work,HH14,this work
CY Tau	3515	-0.58	-0.597	128.4	1.16	cTTS	Luh17+HH14,HH14,JK07
DE Tau	3515	-0.28	-0.308	126.9	1.12	cTTS	Luh17+HH14,HH14,JK07
DF Tau	3560	-0.04	-0.142	124.5	2.9	cTTS	Luh17+HH14,HH14,JK07
DG Tau	4020	-0.29	-0.418	120.8	2.55	cTTS	Luh17+HH14,HH14,JK07
DH Tau	3515	-0.66	-0.693	134.8	2.68	cTTS	Luh17+HH14,HH14,JK07
DK Tau	3900	-0.27	-0.347	128.1	2.64	cTTS	Luh17+HH14,HH14,JK07
DN Tau	3846	-0.08	-0.159	127.8	0.54	cTTS	Luh17+HH14,HH14,JK07
GG Tau	3960	0.15	0.15	140 ^b	1.24	cTTS	Luh17+HH14,HH14,JK07
GI Tau	3828	-0.25	-0.314	130.0	2.73	cTTS	Luh17+HH14,HH14,JK07
GK Tau	4068	-0.03	-0.103	128.8	2.28	cTTS	Luh17+HH14,HH14,JK07
GM Aur	4115	-0.31	-0.200	159.0	2.22	cTTS	Luh17+HH14,HH14,JK07
T Tau	4870	0.85	0.831	143.7	2.37	cTTS	Luh17+HH14,HH14,JK07
Hubble 4	3960	0.04	0.002	125.4	2.5	wTTS	Luh17+HH14,HH14,JK04
WL 17	3400	0.255	0.203	136.5	2.9	class I	D05,D05,JK09
TWA 5A	3410	-0.61	-0.605	49.3	4.9	wTTS	Luh17+HH14,HH14,Y08
TWA 7	3355	-0.94	-0.940	34.0	2.3	wTTS	Luh17+HH14,HH14,Y08
TWA 8A	3355	-0.96	-0.897	46.2	3.3	wTTS	Luh17+HH14,HH14,Y08
TWA 9A	4115	-0.83	-0.410	76.2	3.5	wTTS	HH14,HH14,Y08
TWA 9B	3322	-1.38	-1.046	76.4	3.1	wTTS	HH14,HH14,Y08
TWA Hya	3800	-0.72	-0.629	60.0	3	cTTS	S18,HH14,S18
2M 05353126	3669	0.184	0.184	400 ^b	2.84	cTTS	DR16,DR16,Y11
V1227 Ori	4200	0.086	-0.079	388.8	2.14	cTTS	Y11,Y11,Y11
2M 05351281	3500	-0.165	-0.296	404.4	1.7	cTTS	Y11,Y11,Y11
V1123 Ori	3986	0.007	-0.005	394.5	2.51	wTTS	DR16,DR16,Y11
OV Ori	4245	0.06	0.039	390.3	1.85	cTTS	DR16,DR16,Y11
V1348 Ori	3694	-0.101	-0.123	390.0	3.14	cTTS	DR16,DR16,Y11
LO Ori	3600	-0.051	-0.048	401.3	3.45	cTTS	DR16,DR16,Y11
V568 Ori	3542	-0.061	-0.092	385.9	1.53	cTTS	DR16,DR16,Y11
LW Ori	3961	0.136	0.142	402.8	1.3	cTTS	DR16,DR16,Y11
V1735 Ori	4532	0.071	0.055	392.8	2.08	wTTS	DR16,DR16,Y11
V1568 Ori	3937	-0.131	-0.131	400 ^b	1.42	wTTS	DR16,DR16,Y11
2M 05361049	4279	-0.02	-0.030	395.4	2.31	cTTS	DR16,DR16,Y11
2M 05350475	3762	-0.119	-0.132	394.3	2.79	cTTS	DR16,DR16,Y11
V1124 Ori	3564	-0.224	-0.326	355.7	2.09	wTTS	DR16,DR16,Y11
CHXR 28	4060	0.08	0.283	202.1	1.5	wTTS	Lav17,D13,Lav17
YLW 19	4590	0.12	0.199	142.3	0.8	cTTS	Lav17,E11,Lav17
KM Ori	4730	1.0	0.954	392.5	1.9	wTTS	Lav17,DR12,Lav17
V2062 Oph	4730	0.3	0.164	145.3	1.8	cTTS	Lav17,B92,Lav17

Notes.

^a Distances are from *Gaia* measurements (Bailer-Jones et al. 2018).

^b *Gaia* distance not available, and thus the distance used by the luminosity reference is adopted and the luminosity unchanged.

^c References: B92 = Bouvier & Appenzeller (1992), D05 = Dopmann et al. (2005), D13 = Daemgen et al. (2013), DR12 = Da Rio et al. (2012), DR16 = Da Rio et al. (2016), E11 = Erickson et al. (2011), JK04 = Johns-Krull et al. (2004), JK07 = Johns-Krull (2007), JK09 = Johns-Krull et al. (2009), Lav17 = Lavail et al. (2017), Y08 = Yang et al. (2008), Y11 = Yang & Johns-Krull (2011).

We can plot this maximum field strength for a fully convective star by inputting the evolutionary track predictions at the convective boundary. To minimize the impact of assumptions being made and simplify the complex physical relationships, we can use a reference star and base trends off this reference. The ideal reference star should also be a TTS at the convective boundary. We choose GM Aur from our sample because it is near the fully convective boundary as predicted by both evolutionary models plotted in the HR diagrams (Figure 7). Thus for the reference mass and radius used to approximate the convective boundary in the B versus T_{eff} plot, we adopt the stellar mass and radius that correspond to the

formation of a radiative core in the closest evolutionary track to the position GM Aur in the HR diagrams (model dependent). This choice does impact the vertical placement of this rough boundary, which is most sensitive to the radius. Regardless, we plot the resulting relative maximum magnetic field strength of an equipartition field at the formation of the radiative core in Figure 9. The dashed and dotted lines are the result of inputting the Baraffe or YaPSI model values at the convective boundary (dashed lines in the HR diagrams) into Equation (1). The coherence of the observed data near the plotted boundary is remarkable, especially given the expected uncertainties on the stellar parameters plotted. This plot is suggestive that there is

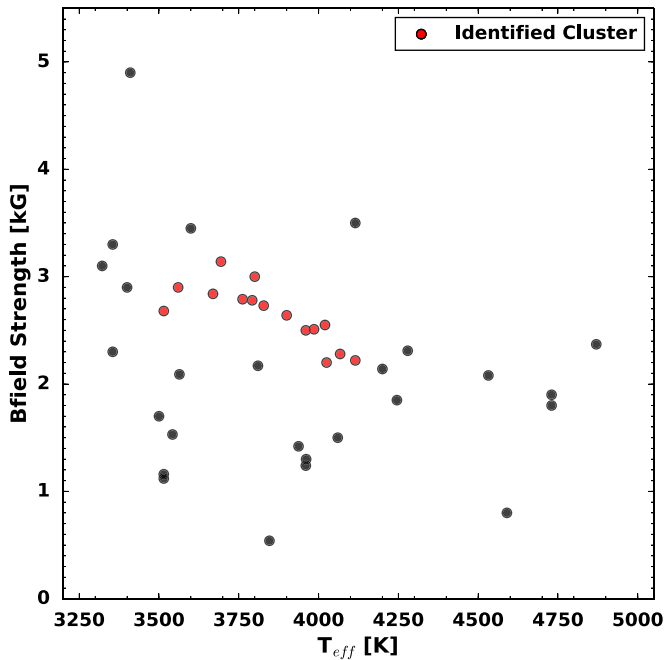


Figure 10. A data cluster identified by fitting the DBSCAN clustering algorithm to the literature data, which matches well with the majority of our by-eye identified source pileup. The Spearman correlation coefficient for this pileup group is $\rho = -0.8$, and is suggestive that the effective temperature and mean magnetic field strength are correlated.

likely a physical change in the generation of the magnetic field that leads to the trend seen in Figure 9, which is related to the stellar structure or age.

The origin of strong magnetic fields for young TTSs is not yet agreed upon. Broadly speaking, the two possible origins for the field are some sort of dynamo action or fossil fields left over from the star formation process. Early inquiries into the equipartition field found that surface convection should be largely suppressed with the large kG magnetic field strengths that are observed, as discussed in Johns-Krull & Valenti (2000), Johns-Krull (2007), and earlier in this paper when discussing Figure 8. While recent simulations of dynamo action in fully convective stars do not find complete suppression of convection by the field in the simulation zone (e.g., Yadav et al. 2015a, 2015b), these simulations are not able to extend all the way to the visible photosphere where the gas pressure decreases dramatically. Therefore, it is likely the observed large field strengths have a substantial effect on convection in the visible photosphere, even if there is strong convection below the photosphere. Additionally, there is a lack of clear correlation in TTS magnetic field data with typical dynamo indicators (e.g., rotation period, convective turnover time, Rossby number) that would indicate a dynamo field generation process is active (e.g., Johns-Krull 2007; Vidotto et al. 2014; Folsom et al. 2016). However, this lack of correlation may be attributed to star-disk interactions or dynamo saturation, as with M dwarfs (Reiners et al. 2009). Furthermore, while it is generally assumed the magnetic field of M stars are dynamo driven, the strength of the magnetic field in some late M stars is greater than expected from saturation in a standard dynamo (e.g., Shulyak et al. 2017), similar to what is seen in TTSs. Meanwhile, a recent non-ideal magnetohydrodynamics simulation shows that a fossil field cannot reproduce the kG magnetic fields that are observed, although resolution may be impacting

this result (Wurster et al. 2018). Further into the TTS evolution, it has been suggested that surface magnetic fields of TTSs could be linked with internal stellar structure. Studies of the magnetic field topology of TTSs, such as the MaPP and MaTYSSSE projects (e.g., Donati et al. 2013; Hill et al. 2017), suggest that the magnetic fields become more complex with age and appear to correlate with internal structure. From this viewpoint, Gregory et al. (2012) proposed that the topology of the magnetic field may even be inferred from the star’s location on the HR diagram, assuming a dynamo-generated field. Regardless of the origin or regulating magnetic process, it seems reasonable that there could be an evolutionary pileup of magnetic field measurements if a dynamo is formed or significantly altered at some evolutionary stage, and that may be what is shown in Figure 9.

Perhaps we are witnessing the conversion from a primordial magnetic field to a dynamo or from one form of dynamo to another (such as a distributed convective dynamo to a solar-like dynamo). It is quite plausible that the trend seen in Figure 9 represents a maximal efficiency of a convective dynamo, which would explain a pileup at the convective boundary. The most straightforward application goes hand-in-hand with the convective boundary if the trend is caused by a conversion to a solar-like (α - ω) dynamo, where the formation of a radiative core could enable the formation of a tachocline. With the development of a core, there is a new source of shear that will magnify the strength of the magnetic field. Thus, a radiative core may boost the magnetic field strength past this rough boundary/trend where the convective limits on the magnetic field no longer hold or are weakened.

Ultimately, the sample that we plot in Figure 9 is rather small and therefore might be exaggerating, or even masquerading as, a trend. A larger sample of sources is needed, particularly at the more evolved stages for lower mass stars, and at less evolved stages for higher mass stars, to verify the seemingly clear separation of fully convective versus stars forming a radiative core/younger versus older stars, as seen with current data. Additionally, as mentioned in the introduction, the very presence of such strong magnetic fields may alter the estimated effective temperature and placement in the HR diagram when not accounted for.

5. Conclusions

Using IGRINS observations of CI Tau, we present an extremely high signal-to-noise combined spectrum that spans from 1.5 to 2.5 μm and has a spectral resolving power of $R = 45,000$. At these NIR wavelengths, the Zeeman effect is enhanced compared to the optical. This broadening is evident in the magnetically sensitive Ti I lines near 2.2 μm in the spectrum of CI Tau and is clearly the result of a strong magnetic field present in this young star. We measure the mean surface magnetic field strength of CI Tau to be $B \approx 2.25$ kG using a blind comparison of two different modeling techniques.

CI Tau appears to be a perfectly ordinary TTS in the context of this paper. Its mean surface magnetic field strength is similar to other TTSs nearby in the HR diagram. Interestingly, we find that plotting the mean surface magnetic field strength versus the effective temperature for TTSs results in an apparent trend suggestive of some physical change. Whether the observed trend is related to the convective boundary, a switch from primordial to dynamo magnetic fields, coincidence, or something else remains to be determined and further evidence is

needed. Regardless, these findings are promising and the implications for future work is exciting.

We thank the anonymous referee for their insightful comments that have improved the paper. K.R.S. would like to thank Dr Casey Deen for assistance with his MoogStokes code. This work used the Immersion Grating Infrared Spectrograph (IGRINS) that was developed under a collaboration between the University of Texas at Austin and the Korea Astronomy and Space Science Institute (KASI) with the financial support of the US National Science Foundation under grant AST-1229522 and AST-1702267, of the University of Texas at Austin, and of the Korean GMT Project of KASI. These results made use of the Discovery Channel Telescope at Lowell Observatory. Lowell is a private, non-profit institution dedicated to astrophysical research and public appreciation of astronomy and operates the DCT in partnership with Boston University, the University of Maryland, the University of Toledo, Northern Arizona University and Yale University.

This work has made use of data from the European Space Agency (ESA) mission *Gaia* (<https://www.cosmos.esa.int/gaia>), processed by the *Gaia* Data Processing and Analysis Consortium (DPAC, <https://www.cosmos.esa.int/web/gaia/dpac/consortium>). Funding for the DPAC has been provided by national institutions, in particular the institutions participating in the *Gaia* Multilateral Agreement.

Facility: DCT (IGRINS)—Lowell Observatory’s 4.3 m Discovery Channel Telescope.

Software: IGRINS pipeline package (version 2.1 alpha 3; Lee & Gullikson 2016), MoogStokes (Deen 2013), MARCS (Gustafsson et al. 2008), SYNTHMAG (Piskunov 1999).

ORCID iDs

Kimberly R. Sokal  <https://orcid.org/0000-0002-3621-1155>

Gregory N. Mace  <https://orcid.org/0000-0001-7875-6391>

Jae-Joon Lee  <https://orcid.org/0000-0003-0894-7824>

Daniel T. Jaffe  <https://orcid.org/0000-0003-3577-3540>

References

- Aarnio, A. N., Matt, S. P., & Stassun, K. G. 2013, *AN*, **334**, 77
- Ádámkóvics, M., Glassgold, A. E., & Najita, J. R. 2014, *ApJ*, **786**, 135
- Allard, F., & Hauschildt, P. H. 1995, in *Proc. ESO Workshop, The Bottom of the Main Sequence—and Beyond*, ed. C. G. Tinney (Berlin: Springer), 32
- Almeida, P. V., Gameiro, J. F., Petrov, P. P., et al. 2017, *A&A*, **600**, A84
- Andrews, S. M., Rosenfeld, K. A., Kraus, A. L., & Wilner, D. J. 2013, *ApJ*, **771**, 129
- Bailer-Jones, C. A. L., Rybizki, J., Fouesneau, M., Mantelet, G., & Andrae, R. 2018, *AJ*, **156**, 58
- Bailey, J. I., III, White, R. J., Blake, C. H., et al. 2012, *ApJ*, **749**, 16
- Baraffe, I., Chabrier, G., Allard, F., & Hauschildt, P. H. 1998, *A&A*, **337**, 403
- Baraffe, I., Homeier, D., Allard, F., & Chabrier, G. 2015, *A&A*, **577**, A42
- Barnes, S., Sofia, S., & Pinsonneault, M. 2001, *ApJ*, **548**, 1071
- Baruteau, C., Crida, A., Paardekooper, S.-J., et al. 2014, in *Protostars and Planets VI*, ed. H. Beuther et al. (Tucson, AZ: Univ. Arizona Press), 667
- Bessolaz, N., Zanni, C., Ferreira, J., Keppens, R., & Bouvier, J. 2008, *A&A*, **478**, 155
- Bevington, P. R., & Robinson, D. K. 1992, in *Data Reduction and Error Analysis for the Physical Sciences*, ed. D. Brufordt & S. J. Cotkin (2nd ed.; New York: McGraw Hill), 161
- Biddle, L. I., Johns-Krull, C. M., Llama, J., Prato, L., & Skiff, B. A. 2018, *ApJL*, **853**, L34
- Bouvier, J., Alencar, S. H. P., Harries, T. J., Johns-Krull, C. M., & Romanova, M. M. 2007, in *Protostars and Planets V*, ed. V. B. Reipurth, D. Jewitt, & K. Keil (Tucson, AZ: Univ. Arizona Press), 479
- Bouvier, J., & Appenzeller, I. 1992, *A&AS*, **92**, 481
- Bouvier, J., Forestini, M., & Allain, S. 1997, *A&A*, **326**, 1023
- Calvet, N., & Gullbring, E. 1998, *ApJ*, **509**, 802
- Cauley, P. W., Johns-Krull, C. M., Hamilton, C. M., & Lockhart, K. 2012, *ApJ*, **756**, 68
- Chabrier, G., Gallardo, J., & Baraffe, I. 2007, *A&A*, **472**, L17
- Chabrier, G., Johansen, A., Janson, M., & Rafikov, R. 2014, in *Protostars and Planets VI*, ed. H. Beuther et al. (Tucson, AZ: Univ. Arizona Press), 619
- Chang, S.-H., Gu, P.-G., & Bodenheimer, P. H. 2010, *ApJ*, **708**, 1692
- Christensen, U. R., Holzwarth, V., & Reiners, A. 2009, *Natur*, **457**, 167
- Cieza, L., & Baliber, N. 2007, *ApJ*, **671**, 605
- Clarke, C. J., Tazzari, M., Juhasz, A., et al. 2018, *ApJL*, **866**, L6
- Crockett, C. J., Mahmud, N. I., Prato, L., et al. 2012, *ApJ*, **761**, 164
- Cushing, M. C., Marley, M. S., Saumon, D., et al. 2008, *ApJ*, **678**, 1372
- Da Rio, N., Robberto, M., Hillenbrand, L. A., Henning, T., & Stassun, K. G. 2012, *ApJ*, **748**, 14
- Da Rio, N., Tan, J. C., Covey, K. R., et al. 2016, *ApJ*, **818**, 59
- Daemgen, S., Petr-Gotzens, M. G., Correia, S., et al. 2013, *A&A*, **554**, A43
- David, T. J., Hillenbrand, L. A., Petigura, E. A., et al. 2016, *Natur*, **534**, 658
- Deen, C. P. 2013, *AJ*, **146**, 51
- Desort, M., Lagrange, A.-M., Galland, F., Udry, S., & Mayor, M. 2007, *A&A*, **473**, 983
- Donati, J.-F., Gregory, S. G., Alencar, S. H. P., et al. 2013, *MNRAS*, **436**, 881
- Donati, J. F., Moutou, C., Malo, L., et al. 2016, *Natur*, **534**, 662
- Doppmann, G. W., Greene, T. P., Covey, K. R., & Lada, C. J. 2005, *AJ*, **130**, 1145
- Doppmann, G. W., & Jaffe, D. T. 2003, *AJ*, **126**, 3030
- Doppmann, G. W., Jaffe, D. T., & White, R. J. 2003, *AJ*, **126**, 3043
- Dullemond, C. P., & Monnier, J. D. 2010, *ARA&A*, **48**, 205
- Edwards, S., Fischer, W., Hillenbrand, L., & Kwan, J. 2006, *ApJ*, **646**, 319
- Edwards, S., Strom, S. E., Hartigan, P., et al. 1993, *AJ*, **106**, 372
- Elsner, R. F., & Lamb, F. K. 1977, *ApJ*, **215**, 897
- Erickson, K. L., Wilking, B. A., Meyer, M. R., Robinson, J. G., & Stephenson, L. N. 2011, *AJ*, **142**, 140
- Ester, M., Kriegl, H. P., Sander, J., & Xu, X. 1996, in *Proc. 2nd Int. Conf. on Knowledge Discovery and Data Mining* (Palo Alto, CA: AAAI Press), 226
- Feiden, G. A. 2016, *A&A*, **593**, A99
- Feiden, G. A., & Chaboyer, B. 2013, *ApJ*, **779**, 183
- Feiden, G. A., & Chaboyer, B. 2014, *ApJ*, **789**, 53
- Folsom, C. P., Petit, P., Bouvier, J., et al. 2016, *MNRAS*, **457**, 580
- Gagné, J., Plavchan, P., Gao, P., et al. 2016, *ApJ*, **822**, 40
- Gallet, F., & Bouvier, J. 2013, *A&A*, **556**, A36
- Gallet, F., & Bouvier, J. 2015, *A&A*, **577**, A98
- Ghosh, P., & Lamb, F. K. 1979, *ApJ*, **232**, 259
- Glassgold, A. E., Najita, J., & Igea, J. 1997, *ApJ*, **480**, 344
- Glassgold, A. E., Najita, J., & Igea, J. 2004, *ApJ*, **615**, 972
- Gray, D. F. 2005, *The Observation and Analysis of Stellar Photospheres* (3rd ed.; Cambridge: Cambridge Univ. Press)
- Greene, T. P., Tokunaga, A. T., Toomey, D. W., & Carr, J. B. 1993, *Proc. SPIE*, **1946**, 313
- Gregory, S. G., Donati, J.-F., Morin, J., et al. 2012, *ApJ*, **755**, 97
- Guilloteau, S., Simon, M., Piétu, V., et al. 2014, *A&A*, **567**, A117
- Gustafsson, B., Edvardsson, B., Eriksson, K., et al. 2008, *A&A*, **486**, 951
- Haisch, K. E., Jr., Lada, E. A., & Lada, C. J. 2001, *ApJL*, **553**, L153
- Hartigan, P., Edwards, S., & Ghandour, L. 1995, *ApJ*, **452**, 736
- Hartmann, L. 1998, *Accretion Processes in Star Formation* (Cambridge: Cambridge Univ. Press)
- Heller, R. 2018, *A&A*, **628**, A42
- Herczeg, G. J., & Hillenbrand, L. A. 2014, *ApJ*, **786**, 97
- Hernández, J., Hartmann, L., Megeath, T., et al. 2007, *ApJ*, **662**, 1067
- Hernán-Obispo, M., Gálvez-Ortiz, M. C., Anglada-Escudé, G., et al. 2010, *A&A*, **512**, A45
- Hill, C. A., Carmona, A., Donati, J.-F., et al. 2017, *MNRAS*, **472**, 1716
- Huélamo, N., Figueira, P., Bonfils, X., et al. 2008, *A&A*, **489**, L9
- Ida, S., & Lin, D. N. C. 2010, *ApJ*, **719**, 810
- Irwin, J., Hodgkin, S., Aigrain, S., et al. 2008, *MNRAS*, **384**, 675
- Johansen, A., Blum, J., Tanaka, H., et al. 2014, in *Protostars and Planets VI*, ed. H. Beuther et al. (Tucson, AZ: Univ. Arizona Press), 547
- Johns-Krull, C. M. 2007, *ApJ*, **664**, 975
- Johns-Krull, C. M., & Gafford, A. D. 2002, *ApJ*, **573**, 685
- Johns-Krull, C. M., Greene, T. P., Doppmann, G. W., & Covey, K. R. 2009, *ApJ*, **700**, 1440
- Johns-Krull, C. M., McLane, J. N., Prato, L., et al. 2016, *ApJ*, **826**, 206
- Johns-Krull, C. M., & Valenti, J. A. 2000, in *ASP Conf. Ser. 198, Stellar Clusters and Associations: Convection, Rotation, and Dynamos*, ed. R. Pallavicini, G. Micela, & S. Sciortino (San Francisco, CA: ASP), 371

- Johns-Krull, C. M., Valenti, J. A., & Koresko, C. 1999, *ApJ*, **516**, 900
- Johns-Krull, C. M., Valenti, J. A., & Saar, S. H. 2004, *ApJ*, **617**, 1204
- Kaltenegger, L., Eiroa, C., Ribas, I., et al. 2010, *AsBio*, **10**, 103
- Krishnamurthi, A., Pinsonneault, M. H., Barnes, S., & Sofia, S. 1997, *ApJ*, **480**, 303
- Kupka, F., Piskunov, N., Ryabchikova, T. A., Stempels, H. C., & Weiss, W. W. 1999, *A&AS*, **138**, 119
- Lagrange, A.-M., Meunier, N., Chauvin, G., et al. 2013, *A&A*, **559**, A83
- Lavail, A., Kochukhov, O., Hussain, G. A. J., et al. 2017, *A&A*, **608**, A77
- Lee, J.-J., & Gullikson, K. 2016, plp: v2.1 alpha 3, Zenodo, doi:10.5281/zenodo.56067
- Lin, D. N. C., Bodenheimer, P., & Richardson, D. C. 1996, *Natur*, **380**, 606
- Lin, D. N. C., & Papaloizou, J. 1986, *ApJ*, **309**, 846
- Luhman, K. L., Mamajek, E. E., Shukla, S. J., & Loutrel, N. P. 2017, *AJ*, **153**, 46
- MacDonald, J., & Mullan, D. J. 2009, *ApJ*, **700**, 387
- Mace, G., Kim, H., Jaffe, D. T., et al. 2016, *Proc. SPIE*, **9908**, 99080C
- Mace, G., Sokal, K., Lee, J.-J., et al. 2018, *Proc. SPIE*, **10702**, 107020Q
- Mahmud, N. I., Crockett, C. J., Johns-Krull, C. M., et al. 2011, *ApJ*, **736**, 123
- Matt, S., & Pudritz, R. E. 2005, *MNRAS*, **356**, 167
- Matt, S. P., Brun, A. S., Baraffe, I., Bouvier, J., & Chabrier, G. 2015, *ApJL*, **799**, L23
- Matt, S. P., Pinzón, G., de la Reza, R., & Greene, T. P. 2010, *ApJ*, **714**, 989
- McClure, M. K., D'Alessio, P., Calvet, N., et al. 2013, *ApJ*, **775**, 114
- Mullan, D. J., & MacDonald, J. 2001, *ApJ*, **559**, 353
- Naoz, S., Farr, W. M., Lithwick, Y., Rasio, F. A., & Teysandier, J. 2011, *Natur*, **473**, 187
- Nguyen, D. C., Brandeker, A., van Kerkwijk, M. H., & Jayawardhana, R. 2012, *ApJ*, **745**, 119
- Padgett, D. L. 1996, *ApJ*, **471**, 847
- Papaloizou, J. C. B., Nelson, R. P., Kley, W., Masset, F. S., & Artymowicz, P. 2007, in *Protostars and Planets V*, ed. B. Reipurth, D. Jewitt, & K. Keil (Tucson, AZ: Univ. Arizona Press), 655
- Park, C., Jaffe, D. T., Yuk, I.-S., et al. 2014, *Proc. SPIE*, **9147**, 91471D
- Paulson, D. B., & Yelda, S. 2006, *PASP*, **118**, 706
- Pecaut, M. J., Mamajek, E. E., & Bubar, E. J. 2012, *ApJ*, **746**, 154
- Pedregosa, F., Varoquaux, G., Gramfort, A., et al. 2011, *J. Mach. Learn. Res.*, **12**, 2825
- Piskunov, N. 1999, in *Solar Polarization*, ed. K. N. Nagendra & J. O. Stenflo (Dordrecht: Springer), 515
- Plavchan, P., & Bilinski, C. 2013, *ApJ*, **769**, 86
- Prato, L., Huerta, M., Johns-Krull, C. M., et al. 2008, *ApJL*, **687**, L103
- Raymond, S. N., Kokubo, E., Morbidelli, A., Morishima, R., & Walsh, K. J. 2014, in *Protostars and Planets VI*, ed. H. Beuther et al. (Tucson, AZ: Univ. Arizona Press), 595
- Rebull, L. M. 2001, *AJ*, **121**, 1676
- Rebull, L. M., Stauffer, J. R., Megeath, S. T., Hora, J. L., & Hartmann, L. 2006, *ApJ*, **646**, 297
- Reiners, A., Basri, G., & Browning, M. 2009, *ApJ*, **692**, 538
- Romanova, M. M., Ustyugova, G. V., Koldoba, A. V., & Lovelace, R. V. E. 2009, *MNRAS*, **399**, 1802
- Saar, S. 1991, in *IAU Colloq. 130, The Sun and Cool Stars. Activity, Magnetism, Dynamos*, ed. I. Tuominen, D. Moss, & G. Rüdiger (Berlin: Springer), 389
- Saar, S. H. 1994, in *IAU Symp. 154, Infrared Solar Physics*, ed. D. M. Rabin, J. T. Jefferies, & C. Lindsey (Dordrecht: Kluwer), 437
- Saar, S. H., & Linsky, J. L. 1985, *ApJL*, **299**, L47
- Santos, N. C., Melo, C., James, D. J., et al. 2008, *A&A*, **480**, 889
- Segura, A., Walkowicz, L. M., Meadows, V., Kasting, J., & Hawley, S. 2010, *AsBio*, **10**, 751
- Setiawan, J., Henning, T., Launhardt, R., et al. 2008, *Natur*, **451**, 38
- Setiawan, J., Weise, P., Henning, T., et al. 2007, *ApJL*, **660**, L145
- Shu, F., Najita, J., Ostriker, E., et al. 1994, *ApJ*, **429**, 781
- Shulyak, D., Reiners, A., Engeln, A., et al. 2017, *NatAs*, **1**, 0184
- Shulyak, D., Reiners, A., Seemann, U., Kochukhov, O., & Piskunov, N. 2014, *A&A*, **563**, A35
- Skumanich, A. 1972, *ApJ*, **171**, 565
- Snedden, C. A. 1973, PhD thesis, Univ. Texas at Austin
- Sokal, K. R., Deen, C. P., Mace, G. N., et al. 2018, *ApJ*, **853**, 120
- Spada, F., Demarque, P., Kim, Y.-C., Boyajian, T. S., & Brewer, J. M. 2017, *ApJ*, **838**, 161
- Stassun, K. G., Mathieu, R. D., Vrba, F. J., Mazeh, T., & Henden, A. 2001, *AJ*, **121**, 1003
- Tilley, M. A., Segura, A., Meadows, V. S., Hawley, S., & Davenport, J. 2017, *AsBio*, **19**, 64
- Tinker, J., Pinsonneault, M., & Terndrup, D. 2002, *ApJ*, **564**, 877
- Tokunaga, A. T., Toomey, D. W., Carr, J., Hall, D. N. B., & Epps, H. W. 1990, *Proc. SPIE*, **1235**, 131
- Torres, G., Andersen, J., & Giménez, A. 2010, *A&ARv*, **18**, 67
- Triaud, A. H. M. J., Collier Cameron, A., Queloz, D., et al. 2010, *A&A*, **524**, A25
- Uzdensky, D. A., Königl, A., & Litwin, C. 2002, *ApJ*, **565**, 1191
- van Eyken, J. C., Ciardi, D. R., Rebull, L. M., et al. 2011, *AJ*, **142**, 60
- van Eyken, J. C., Ciardi, D. R., von Braun, K., et al. 2012, *ApJ*, **755**, 42
- Vidotto, A. A., Gregory, S. G., Jardine, M., et al. 2014, *MNRAS*, **441**, 2361
- Weber, E. J., & Davis, L., Jr. 1967, *ApJ*, **148**, 217
- Wurster, J., Bate, M. R., & Price, D. J. 2018, *MNRAS*, **481**, 2450
- Wyatt, M. C. 2008, *ARA&A*, **46**, 339
- Yadav, R. K., Christensen, U. R., Morin, J., et al. 2015a, *ApJL*, **813**, L31
- Yadav, R. K., Gastine, T., Christensen, U. R., & Reiners, A. 2015b, *A&A*, **573**, A68
- Yang, H., & Johns-Krull, C. M. 2011, *ApJ*, **729**, 83
- Yang, H., Johns-Krull, C. M., & Valenti, J. A. 2005, *ApJ*, **635**, 466
- Yang, H., Johns-Krull, C. M., & Valenti, J. A. 2008, *AJ*, **136**, 2286
- Yu, L., Donati, J.-F., Hébrard, E. M., et al. 2017, *MNRAS*, **467**, 1342
- Zanni, C., & Ferreira, J. 2013, *A&A*, **550**, A99
- Zwillinger, D., & Kokoska, S. 2000, *CRC Standard Probability and Statistics Tables and Formulae* (Boca Raton, FL: CRC Press)